Journal of Materials Science: Materials in Electronics (2019) 30:332–339
https://doi.org/10.1007/s10854-018-0297-1

The effect of the triangular and spherical shaped $CuSbS_2$ structure on the electrical properties of Au/$CuSbS_2$/*p*-Si photodiode

Murat Yıldırım[1] · Adem Kocyigit[2] · Adem Sarılmaz[3] · Faruk Ozel[3,4]

Received: 11 September 2018 / Accepted: 26 October 2018 / Published online: 29 October 2018

Abstract
$CuSbS_2$ (Chalcostibite) crystals were synthesized by the hot-injection method as triangular and spherical shaped structures. The crystals were inserted by spin coating technique as interfacial layers between Au metal and *p*-Si to investigate their electrical and photoresponse properties via *I-V* measurements under various light intensities. The XRD measurements were performed to show the crystalline structure of the spherical and triangular $CuSbS_2$. The TEM images confirmed the triangular and spherical particle structures of the $CuSbS_2$ crystals. The *I-V* measurements were performed under dark, 20–100 mW light intensities with 20 mW interval for spherical and triangular $CuSbS_2$ photodiodes. In addition, diode parameters were extracted and discussed in the details. The results highlighted that triangular and spherical shaped structures have good photoresponse to the illumination and can be employed in the photodiode and photodetector applications.

1 Introduction

Chalcostibite ($CuSbS_2$) is new kind of promising material for thin film solar cells as a good absorber because it has suitable band gap energy value between 1.3 and 1.5 for photovoltaic applications and optical absorption coefficient of 10^4 cm^{-1} [1]. In addition, the $CuSbS_2$ is environmentally friendly, abundant, stable phase and cheap material [2, 3]. These properties of $CuSbS_2$ make it optimum material for photovoltaic absorber [4, 5]. There are many papers with increasing trend about the $CuSbS_2$ recently in the literature, and the papers usually aimed to employ $CuSbS_2$ for optoelectronic applications [6–13]. Kang et al. [7] synthesized $CuSbS_2$ thin films by reactive co-sputtering technique and investigated physical properties. In addition, they fabricated solar cells by employing $CuSbS_2$. Sivagami et al.[8] obtained $CuSbS_2$ nanobrick thin films by the solvothermal method and confirmed the purity of the films and then investigated photoresponse behaviors. Dekhil et al.[13] synthesized $CuSbS_2$ nanopowders by hydrothermal method and studied by various instruments to see the compatibility of the $CuSbS_2$ nanopowders for photovoltaic applications.

Many techniques have been performed to fabricate as film or particle form of the $CuSbS_2$ such as spray pyrolysis [14], chemical bath deposition [15], SILAR [16], electrodeposition [17] and hot-injection techniques [18]. Among them, hot-injection technique provides to obtain good crystalline structures and narrow size distribution [19]. Various shaped is really important because various forms of the $CuSbS_2$ can help to improve the thin film solar cells or optoelectronic applications [20].

Metal and semiconductor contacts can be thought as optoelectronic applications because the light causes electron–hole pairs at the interface when hit the contact [21–23]. When the electrons and holes jump the barrier of the metal–semiconductor contact, there is an increase at the current values that pass through to the contacts. These properties most of the time are used for photodiode or photodetector applications [24, 25]. However, the absorption of the light is really important for light conversion efficiency of the contacts [26]. The $CuSbS_2$ crystals structures can improve

✉ Murat Yıldırım
muratyildirim@selcuk.edu.tr

✉ Faruk Ozel
farukozell@gmail.com

1 Faculty of Science, Department of Biotechnology, Selcuk University, 42030 Konya, Turkey

2 Engineering Faculty, Department of Electrical Electronic Engineering, Igdir University, 76000 Igdir, Turkey

3 Faculty of Engineering, Department of Metallurgical Science and Materials Engineering, Karamanoğlu Mehmetbey University, 70200 Karaman, Turkey

4 KaramanogluMehmetbey University, Scientific and Technological Research and Application Center, 70200 Karaman, Turkey

the light absorption of metal–semiconductor contacts as an interfacial layer for photodiode and photodetector applications [4]. In addition, the shape or structure of the $CuSbS_2$ can affect the behaviors of these photodiode/photodetectors. The aim of this study is to compare and understand the various $CuSbS_2$ structures how to affect the photodiode properties of the metal–semiconductor devices.

In this study, we synthesized triangular and spherical structures of the $CuSbS_2$ by hot-injection method and inserted the structures as thin film form by spin coating technique between the Au metal and *p*-Si to fabricate Au/$CuSbS_2$/*p*-Si photodiodes. The obtained photodiodes were characterized and compared by XRD, TEM and *I-V* measurements under dark and various light illumination intensities.

2 Experimental details

Copper antimony sulfide nanostructures were synthesized using powder and liquid sulfur source by the hot-injection method. The spherical shaped $CuSbS_2$ crystal synthesis was previously published by our group [27]. Triangular shaped $CuSbS_2$ were synthesized according to a previously described procedure with slight modification [28]. To synthesize $CuSbS_2$ nanostructures, typically, copper (II) acetate (1 mmol), antimony (III) chloride (1 mmol) and oleylamine (15 mL) were added to a 25 mL three-necked, round-bottomed flask with electromagnetic stirring under argon atmosphere at room temperature for 15 min. Then, freshly prepared S-precursor solution (0.26 mL 1-dodecanethiol (1-DDT) and 1.76 mL tert-dodecylmercaptan (t-DDT)) was injected rapidly into the hot reaction mixture under vigorous stirring, which resulted in an immediate color change of the reaction solution to black. Next, the solution was heated to 240 °C and kept at this temperature for 30 min. and cooled down to room temperature. Finally, the nanostructures were precipitated adding a mixture of ethanol and toluene centrifuged at the rate of 3000 r/min for 1 min. The final black precipitate was washed with ethanol to remove residual thiols and acetates.

The (100) *p*-type Si wafer, which had 10 Ω cm, were cut 15 mm x 10 mm pieces and cleaned in acetone and propanol by an ultrasonic cleaner and then HF:H_2O (1:1) solution was prepared and the wafer pieces immersed to the solution to remove impurities and native oxide layer from the surfaces. Aluminum (Al) metal (99.999%) with a thickness of 150 nm was thermally evaporated from the tungsten filament onto the whole back surface of the wafer under a pressure of 2×10^{6} Torr. Then, a low resistivity ohmic contact was followed by a temperature treatment at 500 °C for 5 min in a N_2 atmosphere. The prepared triangular and spherical of the $CuSbS_2$ solutions were coated on glass and Si substrates by the spin coating technique at a spinning rate of 1200 rpm for 60 s with Fytronix SC-500 spin coater. The thickness measurement of the coated triangular and spherical structures of the $CuSbS_2$ thin films has been performed by stylus profilometer Veeco Dektak 150 and the thickness of triangular and spherical structures of the $CuSbS_2$ have been determined as 214 nm and 232 nm respectively. In the end, Au layer which has an area of is 7.85×10^{-2} cm^{-2} was evaporated on triangular and spherical shaped structures film surfaces as rectifying contact. So, Au/$CuSbS_2$/*p*-Si devices were obtained, and schematic presentations of the devices have been shown in Fig. 1. In here, while triangular shaped $CuSbS_2$ used device was called Au/T-$CuSbS_2$/*p*-Si, spherical shaped $CuSbS_2$ crystal used device named as

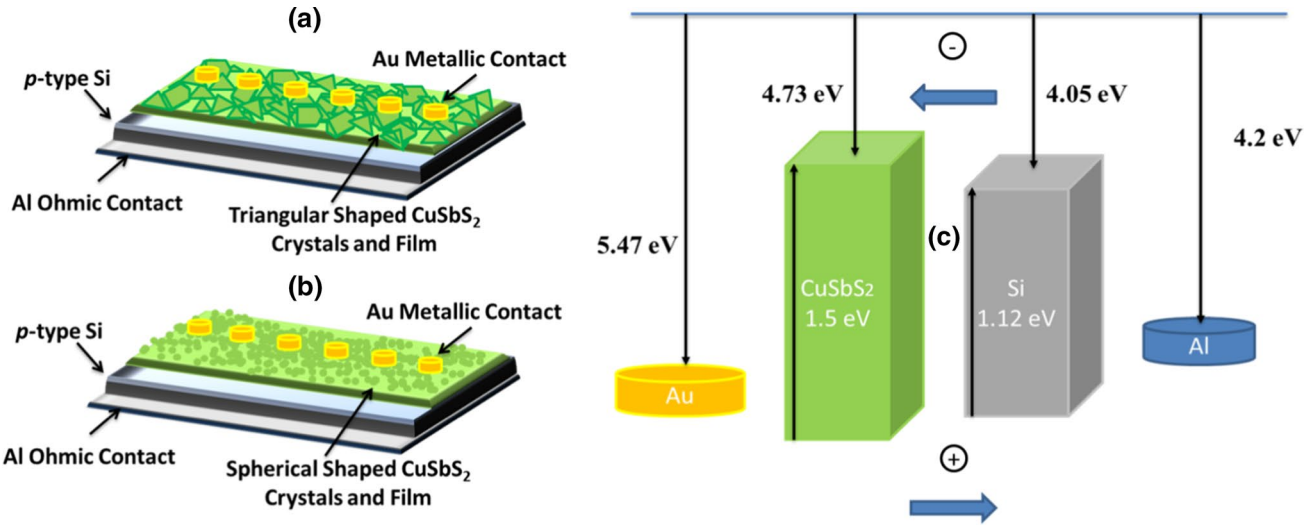

Fig. 1 A kind of schematic presentation of **a** Au/T-$CuSbS_2$/*p*-Si device, **b** Au/S-$CuSbS_2$/*p*-Si device, **c** energy band diagram of the devices

Au/S-$CuSbS_2$/*p*-Si. In addition, schematic energy band diagram of the device have been exhibited in Fig. 1c. The voltage was applied to Au contact for measurements.

Powder X-ray diffraction (XRD) patterns were recorded with a Bruker D8 Advance X-ray (Cu α source with 1.5406 Wavelengths) diffractometer. TEM images were obtained on JEOL JEM-2100F transmission electron microscope (TEM) was used to take the nanostructure images of the crystals. *I-V* and the photovoltaic measurements were performed using by Fytronix FY-5000 photovoltaic characterization system under dark and various light illumination conditions.

3 Results and discussion

3.1 Structural properties

X-ray diffraction (XRD) analysis was employed to identify the crystallographic structure and phase purity of the prepared chalcostibite samples in comparison with those of the triangular and spherical structured samples. The distinctive diffraction peaks for the $CuSbS_2$ can be perfectly indexed as the single crystalline orthorhombic structures of $CuSbS_2$ (PDF No: 01-073-3954) both spherical (Fig. 2a) and triangular (Fig. 2b) shaped structure. Since the synthesized materials are of the same crystalline structure, both of the XRD patterns showed similar results [29]. However, as observed in Fig. 2a, b, the differences in peak intensities are due to different interactions of the surfactants and anions. Moreover, there are no diffraction signals of binary structures on the XRD pattern, which showed that obtained nanostructures had high purity. Figure 2c shows corresponding crystal structure with various directions as schematically.

3.2 Morphological properties

The TEM and SAED images of the T-$CuSbS_2$ and S-$CuSbS_2$ are presented in Fig. 3. According to Fig. 3a, T-$CuSbS_2$ obtained by hot injection reaction mainly exhibits triangular shape with edge lengths ranging from 20 to 120 nm. On the other hand, S-$CuSbS_2$ exhibits a spherical structure with grain size ranges 20–40 nm, possessing a large surface area in Fig. 3b. The differences in the coordination capability of the products using OLA as solvents with the cations and anions could be the reason for the observed alterations in the shape and size of them. SAED images of the nanostructures are given in Fig. 2c, d for T-$CuSbS_2$ and S-$CuSbS_2$, respectively. As presented in Fig. 2c, d, the nanostructures have single crystalline in nature. Further, SAED diffraction spots correspond to chalcostibite structure and these results are compatible with XRD results.

3.3 Electrical properties

The $CuSbS_2$ crystals structure with triangular and spherical shaped were employed as interfacial thin film layer to obtain Au/$CuSbS_2$/*p*-Si devices. To characterize their electrical properties, *I-V* measurements were performed while the devices were under dark and illumination conditions in the range 20 mW-100 mW with 20 mW steps. The *I-V* characteristics of the Au/$CuSbS_2$/*p*-Si devices have been shown in Fig. 4 for interfacial $CuSbS_2$ layers with triangular and spherical shaped structures. The devices exhibited

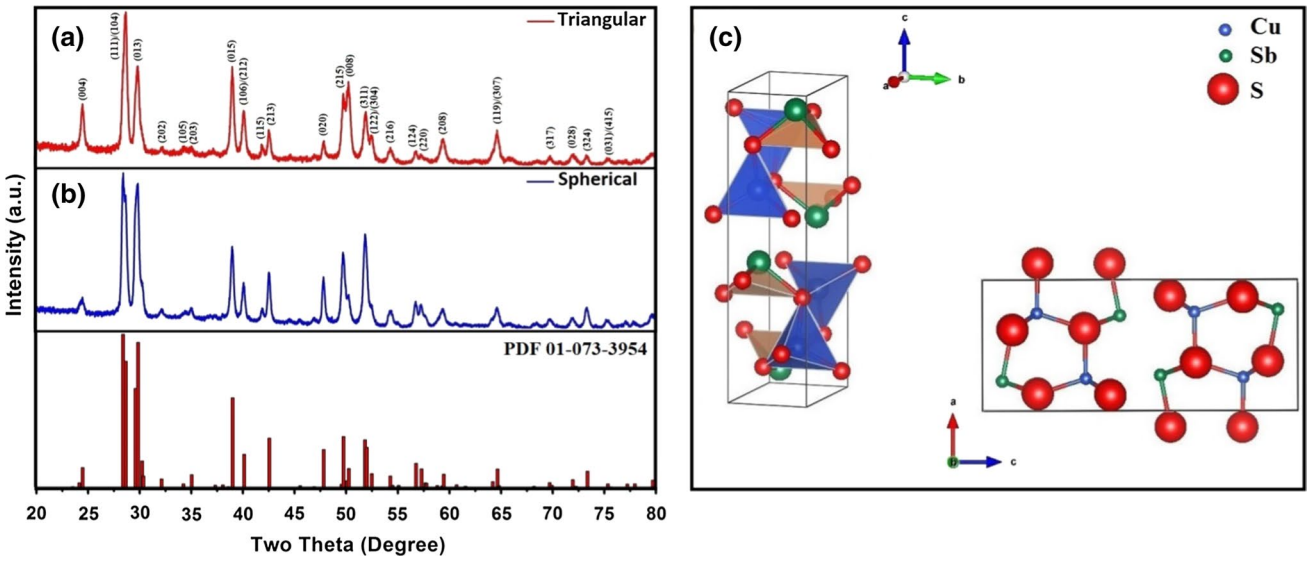

Fig. 2 XRD graphs of the $CuSbS_2$ crystals **a** spherical, **b** triangular-shaped and **c** corresponding crystal structure with different directions as schematically

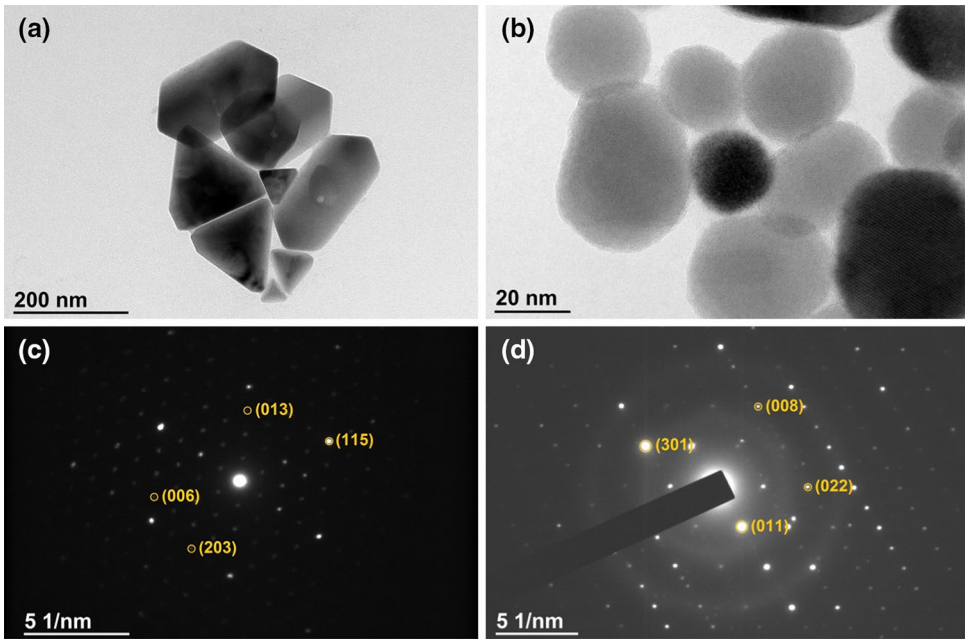

Fig. 3 TEM and SAED images of the $CuSbS_2$: **a** triangular, **b** spherical shaped structures. SAED images of the **c** triangular, **d** spherical shaped $CuSbS_2$ crystals

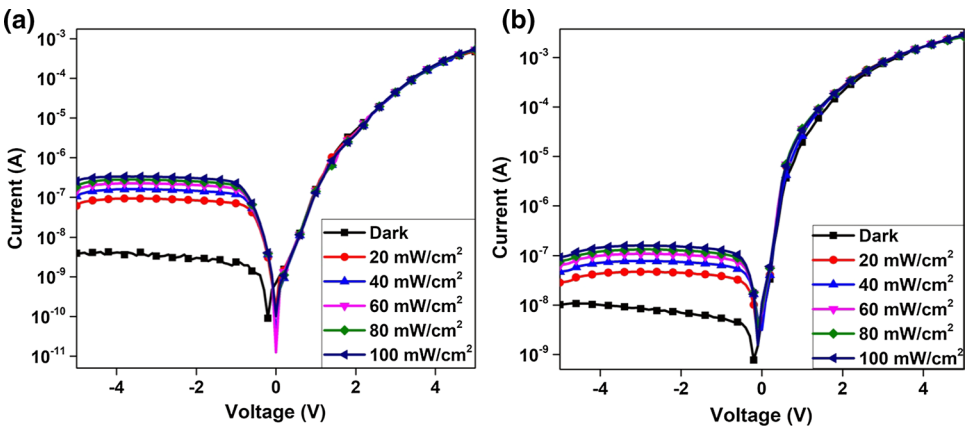

Fig. 4 The *I-V* plots of **a** Au/T-$CuSbS_2$/*p*-Si and **b** Au/S-$CuSbS_2$/*p*-Si devices under dark and various light intensities

good rectifying properties, but Au/S-$CuSbS_2$/*p*-Si has better rectifying behavior than Au/T-$CuSbS_2$/*p*-Si device. The obtained rectifying ratio values of the Au/T-$CuSbS_2$/*p*-Si and Au/S-$CuSbS_2$/*p*-Si devices are 1.37×10^5 and 2.52×10^5, respectively. The calculated rectifying ratio values are comparable with literature [30, 31]. Both devices responded to the light illumination at reverse biases because the current values increased via increasing light intensity. This property caused by the generation of the electron–hole pairs in the interface of the devices owing to light illumination [32]. In addition, The devices can be employed as photodetector and photodiode applications because increasing current values at the reverse biases [33, 34].

The diode parameters can help to understand more the electrical properties of the devices. For that reason, the diode parameters such as barrier height (ϕ_b), ideality factor (n) and series resistance (R_s) should be determined from *I–V* measurements. There is three technique to calculate the diode parameters: thermionic emission theory, Cheung and Norde methods. The current (I) is calculated from *I-V* measurements via the following formula according to thermionic emission theory [35–37]:

$$I = I_0 \exp\left(\frac{qV}{nkT}\right)\left[1 - \exp\left(-\frac{qV}{nkT}\right)\right] \quad (1)$$

where I_0 shows saturation current determined from the linear zone of the *I–V* graph. I_0 also is calculated as the next equation:

$$I_0 = AA^*T^2 \exp\left(-\frac{q\phi_b}{kT}\right) \quad (2)$$

where A, A^* and T indicate diode area (in here A is equal to 7.85×10^{-3} cm^2), Richardson constant (32 A cm^{-2} K^{-2}

for *p*-type Si) and temperature, respectively. q and k represent the charge of electron and Boltzmann's constant. The determined saturation current values for Au/T-$CuSbS_2$/*p*-Si and Au/S-$CuSbS_2$/*p*-Si devices are 1.47×10^{-10} A and 2.75×10^{-10} A, respectively. While the saturation current help to calculate barrier height values, a slope of d*V*/dln*I* provide to determine ideality factors of the devices for $V \geq 3kT/q$ region via relevant formulas shown in below:

$$n = \frac{q}{kT}\left(\frac{dV}{d\ln I}\right) \tag{3}$$

And

$$\phi_b = \frac{kT}{q}\ln\left(\frac{A^*AT^2}{I_0}\right) \tag{4}$$

The ideality factors and barrier height values were accounted for and listed in Table 1 for Au/T-$CuSbS_2$/*p*-Si and Au/S-$CuSbS_2$/*p*-Si devices. While Au/T-$CuSbS_2$/*p*-Si device has 6.96 ideality factor, the Au/S-$CuSbS_2$/*p*-Si has 3.65 lower than triangular shaped $CuSbS_2$ structures. The higher ideality factor values than one can be attributed to various reasons such as barrier inhomogeneity, distribution of the carriers, image force effects and series resistances of the devices [38–40]. The higher ideality factors at these devices can be attributed to barrier inhomogeneity and resistance effects [39, 41]. The differences at the ideality factor values between the Triangular-$CuSbS_2$ and spherical-$CuSbS_2$ devices confirmed the barrier inhomogeneity effect because triangular structure caused more non-uniform distribution as an interfacial layer than particle structures. In addition, *I*–*V* characteristics of the devices were affected from the series (R_s) and shunt resistances (R_{sh}) which are relevant with metal–semiconductor interfacial layer and semiconductor-contact interface, respectively, and they are called junction resistance (R_j) totally [42]. The determining of these parameters is really important to understand the device characteristics [43]. The R_j is given as the following equation:

$$R_j = \frac{\partial V}{\partial I} \tag{5}$$

The determined R_s and R_{sh} values were obtained as 82.2 kΩ and 4.56×10^5 kΩ for Au/T-$CuSbS_2$/*p*-Si device, 2.95 kΩ and 1.34×10^5 kΩ for Au/S-$CuSbS_2$/*p*-Si device. According to these results, both devices have higher R_{sh} values than R_s, and R_{sh} values are 10^8 Ω level. These results made the devices ideal for high performance devices [44].

The conduction mechanism of the Au/T-$CuSbS_2$/*p*-Si and Au/S-$CuSbS_2$/*p*-Si devices should be determined by ln*I*-ln*V* plot because the thermionic emission theory is not effective for high *n* values. The relation between current and voltage is shown $I\alpha V^m$, and the *m*, power-law parameter is determined from the slope of the linear region at ln*I*-ln*V* plot. Thus, the slope of the ln*I*-ln*V* plot refers to the conduction mechanism of the junction. If the slope of the plots higher than two ($m>2$), the space charge limited current (SCLC) mechanism is effective. If *m* is between one and two, Schottky and Poole–Frenkel Conduction are dominant. If *m* is equal to one, the junction has Ohmic character [45].

The ln*I*-ln*V* plots of the Au/T-$CuSbS_2$/*p*-Si and Au/S-$CuSbS_2$/*p*-Si devices have been shown in Fig. 5. While Au/S-$CuSbS_2$/*p*-Si device has SCLC conduction mechanism, the Au/S-$CuSbS_2$/*p*-Si device has Schottky and Poole–Frenkel Conduction for first regions [22]. Poole–Frenkel Conduction referred to that T-$CuSbS_2$ layer started to conduct electricity. In the second and thirds regions of the Au/T-$CuSbS_2$/*p*-Si and Au/S-$CuSbS_2$/*p*-Si devices, the SCLC is dominant conduction mechanism and assigned to that the density of injected free charge is much larger than the

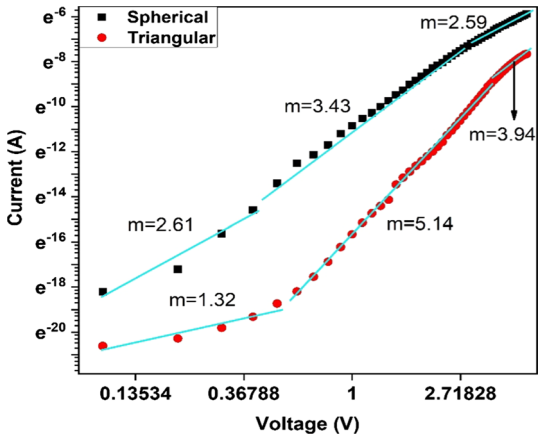

Fig. 5 The ln*I*-ln*V* plots of Au/T-$CuSbS_2$/*p*-Si and Au/S-$CuSbS_2$/*p*-Si devices

Table 1 The diode parameters of the Au/T-$CuSbS_2$/*p*-Si and Au/S-$CuSbS_2$/*p*-Si devices for various methods

Device	Saturation current (I_0)	*n* (*I*–*V*)	*n* Cheung	ϕ_b (*I*–*V*) (eV)	ϕ_b Cheung (eV)	ϕ_b Norde (eV)	R_s Cheung (kΩ (*H*(*I*)))	R_s Cheung [(kΩ (*d*ln*I*)]	R_s Norde (kΩ)
Triangular shaped	1.75×10^{-10}	6.96	7.32	0.85	0.80	0.91	76.50	87.30	21.50
Spherical shaped	2.47×10^{-10}	3.65	4.60	0.83	0.90	0.83	6.18	8.75	6.07

thermal-generated free charge carrier density and increasing current [46].

The second method to calculate the diode parameter is Cheung method, and the method also helps to determine the R_s values. Normally, all the time the metal–semiconductor devices have R_s, but we cannot calculate R_s values through thermionic emission theory.

While Cheung method is performed, the current is written as the next equation including voltage drop at the current because of series resistance:

$$I = I_0 \exp\left(-\frac{q(V - IR_s)}{nkT}\right) \tag{6}$$

In this equation, IR_s represent the voltage drop. While the R_s is left alone at the left side of the Eq. (5), Cheung's functions are transformed to below formula:

$$\frac{dV}{d\ln I} = IR_s + n\frac{kT}{q} \tag{7}$$

$$H(I) = V - n\left(\frac{kT}{q}\right)\ln\left(\frac{I}{AA^*T^2}\right) \tag{8}$$

where $H(I)$ can be written as:

$$H(I) = IR_s + n\phi_b \tag{9}$$

Equations (7) and (9) are called Cheung functions and derived by Cheung and Cheung [47]. While the graphs of Chung functions are plotted versus current, the graphs exhibit straight lines. The dV/dln$I$ versus I graph provides to determine ideality factor from y-intercept and series resistance value from slope. The $H(I)$-I graph is used to determine barrier height from y-intercept and another R_s value from slope. The two R_s values is important for consistency of the Cheung method [48].

Figure 6a, b show the dV/dln$I$ versus I and $H(I)$ versus I graphs of the Au/T-$CuSbS_2$/p-Si and Au/S-$CuSbS_2$/p-Si devices, respectively. The determined n, φ_b and R_s values are listed in Table 1 for two devices. According to Table 1, there is some deviation both ideality factors and barrier heights of the devices. These differences can be ascribed to non-ideal diode structures, non-uniform distribution of the interface structures and approximation differences [48, 49]. Furthermore, there are some differences also at the series resistance values for both devices obtained from dV/dln$I$ versus I and $H(I)$ versus I graphs because of barrier inhomogeneity or native $CuSbS_2$ layers. In addition, The obtained R_s values is comparable R_s values through obtained R_j calculation for both devices.

The alternative method to calculate the series resistance value, as well as barrier height, is Norde method. The function of the Norde method is expressed as below equation [50]:

$$F(V) = \frac{V}{\gamma} - \frac{kT}{q}\ln\left(\frac{I(V)}{AA^*T^2}\right) \tag{10}$$

where γ shows closest integer (dimensionless) value of the ideality factor, n. $I(V)$ represents the currents depending on the voltages. If Eq. (10) is reorganized for φ_b and R_s, next formulas are obtained:

$$\phi_b = F(V_0) + \left[\frac{V_0}{\gamma} - \frac{kT}{q}\right] \tag{11}$$

$$R_s = \frac{\gamma - n}{I}\frac{kT}{q} \tag{12}$$

where V_0 is the minimum voltage value depending on Norde function. Figure 7 displays $F(V)$ versus V graphs of the Au/T-$CuSbS_2$/p-Si and Au/S-$CuSbS_2$/p-Si devices. The

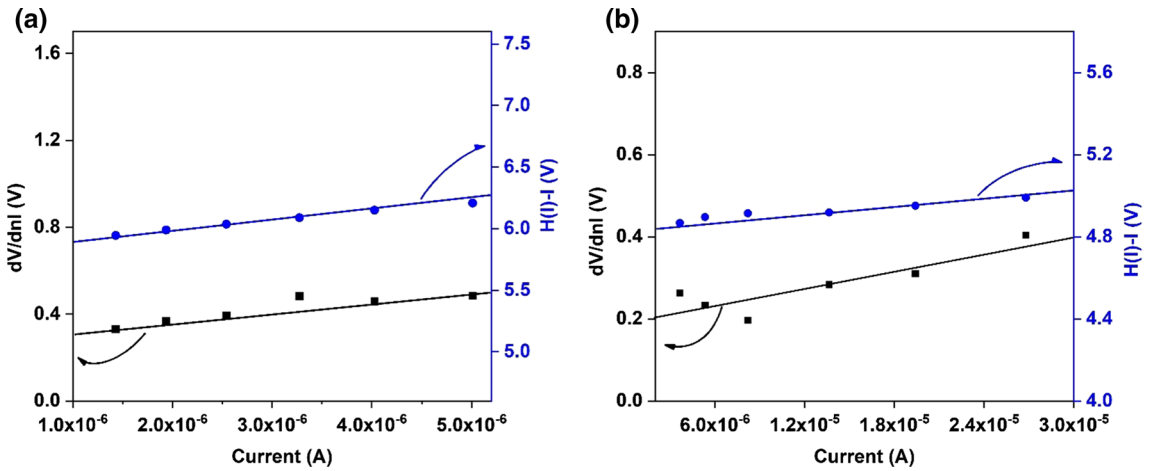

Fig. 6 dV/dln$I$-I and $H(I)$-I graphs of **a** Au/T-$CuSbS_2$/p-Si and **b** Au/S-$CuSbS_2$/p-Si devices

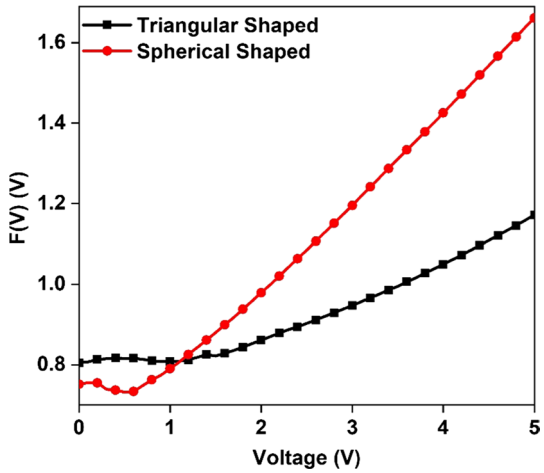

Fig. 7 *F(V)-V* graphs of the Au/T-$CuSbS_2$/*p*-Si and Au/S-$CuSbS_2$/*p*-Si devices

obtained φ_b and R_s values are tabulated in Table 1 for two devices. According to φ_b values, Au/S-$CuSbS_2$/*p*-Si device has smaller φ_b than Au/T-$CuSbS_2$/*p*-Si device. The reason for this case can be attributed to non-uniform distribution of the triangular $CuSbS_2$ structures at the interface layer of the device.

$logI_{ph}$ versus $logP$ plots of the devices have been displayed in Fig. 8a to understand the photoconductive mechanism. The below formula provide to understand the photoconduction mechanism of the photodiodes.

$$I_{ph} = \alpha P^m \tag{13}$$

where I_{ph}, α, P m describe photocurrent, a constant, power of the light and linearity ratio of light power-photocurrent, respectively. According to Fig. 8a, the Au/T-$CuSbS_2$/*p*-Si and Au/S-$CuSbS_2$/*p*-Si devices have linear behavior with increasing light intensity and can be performed as photodetector applications [51]. Figure 8b exhibits photoresponse graph of the Au/T-$CuSbS_2$/*p*-Si and Au/S-$CuSbS_2$/*p*-Si devices. Both devices again have linear photoresponse to the light.

4 Conclusions

We synthesized triangular and spherical shaped structures of the $CuSbS_2$ crystals, separately and employed them as interfacial layer between the Au metal and *p*-type Si to fabricate Au/T-$CuSbS_2$/*p*-Si and Au/S-$CuSbS_2$/*p*-Si devices. The devices were characterized by XRD, TEM and *I-V* measurements. The XRD patterns revealed the crystal structure of the $CuSbS_2$ for both triangular and spherical shaped structures. The difference of two XRD patterns is just intensity changes of the plane peaks. The TEM images confirmed triangular and spherical shaped structure of the $CuSbS_2$ and crystalline structure by SAED images. The *I-V* measurements were performed on the Au/T-$CuSbS_2$/*p*-Si and Au/S-$CuSbS_2$/*p*-Si devices under dark and various light intensities. The diode parameters of the devices were calculated and discussed in the details via comparing the devices. According to diode parameters the spherical form of the $CuSbS_2$ crystals is better than the triangular form of the $CuSbS_2$. This result can be attributed to non-uniform distribution the triangular shapes of $CuSbS_2$ in the interface of the device. The obtained devices can be employed as photodetector and photodiode applications.

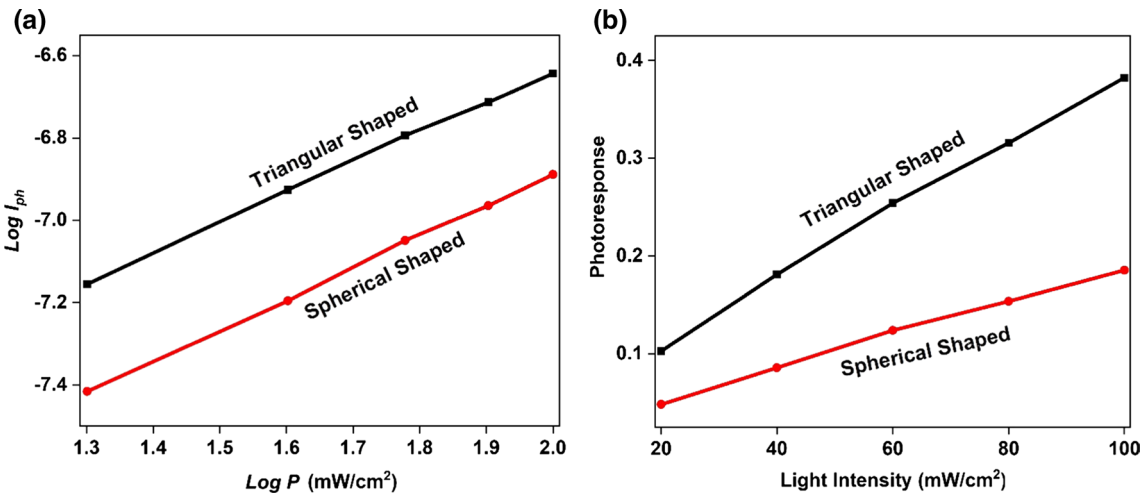

Fig. 8 **a** $logI_{ph}$-$LogP$ and **b** Photoresponse of the Au/T-$CuSbS_2$/*p*-Si and Au/S-$CuSbS_2$/*p*-Si devices

Acknowledgements This work is supported by Selçuk University BAP office with the research Project Number 17401159 and TUBITAK (The Scientific and Technological Research Council of Turkey) under project number 217M212.

References

1. B. Yang, L. Wang, J. Han, Y. Zhou, H. Song, S. Chen, J. Zhong, L. Lv, D. Niu, J. Tang, Chem. Mater. **26**, 3135 (2014)
2. C. Macías, S. Lugo, Á Benítez, I. López, B. Kharissov, A. Vázquez, Y. Peña, Mater. Res. Bull. **87**, 161 (2017)
3. L. Zhang, Y. Li, X. Li, C. Li, R. Zhang, J.J. Delaunay, H. Zhu, Nano Energy **28**, 135 (2016)
4. S. Banu, S.J. Ahn, S.K. Ahn, K. Yoon, A. Cho, Sol. Energy Mater. Sol. Cells **151**, 14 (2016)
5. M. Kumar, C. Persson, J. Renew. Sustain. Energy (American Institute of Physics, College Park, 2013), p. 031616
6. R. Teimouri, R. Mohammadpour, Superlattices Microstruct. **118**, 116 (2018)
7. L. Kang, L. Zhao, L. Jiang, C. Yan, K. Sun, B.K. Ng, C. Gao, F. Liu, Mater. Sci. Semicond. Process. **84**, 101 (2018)
8. A.D. Sivagami, K. Biswas, A. Sarma, Mater. Sci. Semicond. Process. **87**, 69 (2018)
9. U. Chalapathi, B. Poornaprakash, C.H. Ahn, S.H. Park, Ceram. Int. **44**, 14844 (2018)
10. M.E. Edley, B. Opasanont, J.T. Conley, H. Tran, S.Y. Smolin, S. Li, A.D. Dillon, A.T. Fafarman, J.B. Baxter, Thin Solid Films **646**, 180 (2018)
11. W. Wang, L. Hao, W. Zhang, Q. Lin, X. Zhang, Z. Tang, J. Mater. Sci. **29**, 4075 (2018)
12. S. Moosakhani, A.A. Sabbagh Alvani, R. Mohammadpour, P.M. Hannula, Y. Ge, S.P. Hannula, Mater. Lett. **215**, 157 (2018)
13. S. Dekhil, H. Dahman, S. Rabaoui, N. Yaacoub, L. El Mir, J. Mater. Sci. **28**, 11631 (2017)
14. J.A. Ramos Aquino, D.L. Rodriguez Vela, S. Shaji, D.A. Avellaneda, B. Krishnan, Phys. Status Solidi **13**, 24 (2016)
15. Y. Rodríguez-Lazcano, M.T.S. Nair, P.K. Nair, J. Cryst. Growth **223**, 399 (2001)
16. Z. Liu, J. Huang, J. Han, T. Hong, J. Zhang, Z. Liu, Phys. Chem. Chem. Phys. **18**, 16615 (2016)
17. A.C. Rastogi, N.R. Janardhana, Thin Solid Films **565**, 285 (2014)
18. S. Ikeda, S. Sogawa, Y. Tokai, W. Septina, T. Harada, M. Matsumura, RSC Adv. **4**, 40969 (2014)
19. M.-R. Gao, Y.-F. Xu, J. Jiang, S.-H. Yu, Chem. Soc. Rev. **42**, 2986 (2013)
20. K. Ramasamy, H. Sims, W.H. Butler, A. Gupta, J. Am. Chem. Soc. **136**, 1587 (2014)
21. S. Wageh, W.A. Farooq, A. Tataroğlu, A. Dere, A.G. Al-Sehemi, A.A. Al-Ghamdi, F. Yakuphanoglu, Phys. B **527**, 44 (2017)
22. B. Tatar, A.E. Bulgurcuoglu, P. Gokdemir, P. Aydogan, D. Yilmazer, O. ozdemir, K. Kutlu, Int. J. Hydrog. Energy **34**, 5208 (2009)
23. I. Orak, M. Toprak, A. Turut, Phys. Scr. **89**, 115810 (2014)
24. A.S. Dahlan, A. Tataroğlu, A.A. Al-Ghamdi, A.A. Al-Ghamdi, S. Bin-Omran, Y. Al-Turki, F. El-Tantawy, F. Yakuphanoglu, J. Alloys Compd. **646**, 1151 (2015)
25. F. Wang, J. Mei, Y. Wang, L. Zhang, H. Zhao, D. Zhao, ACS Appl. Mater. Interfaces **8**, 2840 (2016)
26. O.S. Cifci, A. Kocyigit, P. Sun, Superlattices Microstruct. **120**, 492 (2018)
27. M. Yıldırım, A. Aljabour, A. Sarılmaz, F. Özel, J. Alloys Compd. **722**, 420 (2017)
28. A. Singh, H. Geaney, F. Laffir, K.M. Ryan, J. Am. Chem. Soc. **134**, 2910 (2012)
29. F. Ozel, E. Aslan, B. Istanbullu, O. Akay, I. Hatay, Patir, Appl. Catal. B. **198**, 67 (2016)
30. M. Soylu, I.S. Yahia, F. Yakuphanoglu, W.A. Farooq, J. Appl. Phys. **110**, 074514 (2011)
31. E.A. Guliants, C. Ji, Y.J. Song, W.A. Anderson, Appl. Phys. Lett. **80**, 1474 (2002)
32. B.A. Gozeh, A. Karabulut, A. Yildiz, F. Yakuphanoglu, J. Alloys Compd. **732**, 16 (2018)
33. S.K. Singh, P. Hazra, S. Tripathi, P. Chakrabarti, Superlattices Microstruct. **91**, 62 (2016)
34. O.S. Cifci, M. Bakir, J.L. Meyer, A. Kocyigit, Mater. Sci. Semicond. Process. **74**, 175 (2018)
35. M. Ilhan, J. Mater. Electron. Devices **1**, 15 (2017)
36. Ş Altındal, J. Mater. Electron. Devices **1**, 42 (2017)
37. H. Özerli, İ Karteri, A. Bekereci, Ş Karataş, J. Mater. Electron. Devices **1**, 83 (2017)
38. B. Roul, S. Mukundan, G. Chandan, L. Mohan, S.B. Krupanidhi, Cit. AIP Adv. Appl. Phys. Lett **5**, 162111 (2015)
39. Ş Karataş, Microelectron. Eng. **87**, 1935 (2010)
40. N.P. Maity, R. Maity, R.K. Thapa, S. Baishya, J. Nanoelectron. Optoelectron. **10**, 645 (2015)
41. D.E. Yıldız, Ş Altındal, H. Kanbur, J. Appl. Phys. **103**, 124502 (2008)
42. F. Yakuphanoglu, S. Actuators, A Phys. **141**, 383 (2008)
43. L.D. Rao, V.R. Reddy, in *AIP Conf. Proc*. (AIP Publishing LLC, 2016), p. 120020
44. İ Taşçıoğlu, W.A. Farooq, R. Turan, Ş Altındal, F. Yakuphanoglu, J. Alloys Compd. **590**, 157 (2014)
45. A. Kaya, E. Marıl, Ş Altındal, İ Uslu, Microelectron. Eng. **149**, 166 (2016)
46. I. Missoum, Y.S. Ocak, M. Benhaliliba, C.E. Benouis, A. Chaker, Synth. Met. **214**, 76 (2016)
47. S.K. Cheung, N.W. Cheung, Appl. Phys. Lett. **49**, 85 (1986)
48. Ş Karataş, N. Yildirim, A. Türüt, Superlattices Microstruct. **64**, 483 (2013)
49. A. Kocyigit, I. Orak, İ Karteri, S. Uruş, Curr. Appl. Phys. **17**, 1215 (2017)
50. H. Norde, J. Appl. Phys. **50**, 5052 (1979)
51. M. Yıldırım, A. Kocyigit, J. Alloys Compd. **768**, 1064 (2018)